

# Focusing iterative migration of gravity gradiometry data acquired in the Nordkapp Basin, Barents Sea

Zhengwei Xu<sup>1</sup>, Le Wan<sup>2,3\*</sup> and Michael S. Zhdanov<sup>2,3,4</sup>

<sup>1</sup>Rock Physics Laboratory, Department of Earth and Atmospheric Sciences, University of Houston, Houston, 77004, USA, <sup>2</sup>Consortium for Electromagnetic Modelling and Inversion (CEMI), The University of Utah, Salt Lake City, UT 84114, USA, <sup>3</sup>TechnoImaging, Salt Lake City, UT, USA, and <sup>4</sup>Moscow Institute of Physics and Technology, Moscow 141700, Russia

Received August 2019, revision accepted May 2020

## ABSTRACT

Geological interpretation based on gravity gradiometry data constitutes a very challenging problem. Rigorous 3D inversion is the main technique used in quantitative interpretation of the gravity gradiometry data. An alternative approach to the quantitative analysis of the gravity gradiometry data is based on 3D smooth potential field migration. This rapid imaging approach, however, has the shortcomings of providing smooth images since it is based on direct integral transformation of the observed gravity tensor data. Another limitation of migration transformation is related to the fact that, in a general case, the gravity data generated by the migration image do not fit the observed data well. In this paper, we describe a new approach to rapid imaging that allows us to produce the density distribution which adequately describes the observed data and, at the same time, images the structures with anomalous densities having sharp boundaries. This approach is based on the basic theory of potential field migration with a focusing stabilizer in the framework of regularized scheme, which iteratively transfers the observed gravity tensor field into an image of the density distribution in the subsurface formations. The results of gravity migration can also be considered as an *a priori* model for conventional inversion subsequently. We demonstrate the practical application of migration imaging using both synthetic and real gravity gradiometry data sets acquired for the Nordkapp Basin in the Barents Sea.

**Key words:** Focusing, Gravity gradiometry, Iterative migration.

## 1 INTRODUCTION

Density distribution provides important information about subsurface geological formations. In hydrocarbon exploration, 3D density models are used for resolving the non-uniqueness problem of recovering seismic velocity from acoustic impedances. In mineral exploration, locating mineralization zones is often dependent on the quantitative interpretation of density properties. There are many methods that use gravity data to explain subsurface density anomalies, such as the direct interpretation of Bouguer anomaly data

and trial-and-error method (Yegorova *et al.*, 1999; An and Assumpção, 2006; Yang *et al.*, 2019). Recovering a 3D density model by 3D inversion of gravity gradiometry data (Dransfield, 2010) is considered as a practical approach to quantitative interpretation. Successful 3D interpretation based on inversion with regularization has been reported in the literature (e.g. Li and Oldenburg, 1998; Li, 2001; Nagihara and Hall, 2001; Zhdanov *et al.*, 2004; Hautot *et al.*, 2007; Işık and Şenel, 2009; Silva Dias *et al.*, 2011; Mammo, 2013; Ren *et al.*, 2018). However, interpretation by 3D inversion can be a complex and time-consuming task involving calculations and transformations of large matrices. In seismic depth conversion workflow, for example, extracting both

---

\*E-mail: le.wan@utah.edu

density and velocity information from acoustic impedance is hampered by non-uniqueness. Generating an independent estimate of density distribution from gravity data can be very helpful in reducing uncertainty in the analysis of the acoustic impedance with respect to density with a proper scaling of seismic images.

Many fast and semi-automated techniques have been developed to solve these problems, such as the Euler deconvolution methods (Thompson, 1982; Stavrev, 1997; Fedi and Florio, 2006), the continuous wavelet transform (Hornby *et al.*, 1999; Sailhac and Gibert, 2003), analytic signal functions (Salem and Ravat, 2003; Smith and Salem, 2005), magnitude magnetic anomaly interpretation (Stavrev, 2006) and the depth-from-extreme points (DEXP) method (e.g. Fedi, 2007; Baniamerian *et al.*, 2016; Liu *et al.*, 2019). Analysis of theoretical responses from specific sources of the potential fields has been the basis of these methods.

A novel approach to rapid imaging of gravity data, based on a one-step 2D and 3D smooth gravity migration, was introduced by Zhdanov (2002) and Zhdanov *et al.* (2010, 2011). The concept of migration in geophysical fields was originally developed for rapid seismic imaging (Schneider, 1978; Claerbout, 1985; Berkhout, 2012). It was demonstrated by Zhdanov (2002, 2009, 2012) that this approach can be applied to geopotential fields, such as gravity tensor field, as well. The migration method enables rapid and stable imaging of sources of potential field anomalies. *A priori* models of the sources of the field, in a general case, are not required for gravity migration (Zhdanov *et al.*, 2011).

A comprehensive review of noniterative imaging methods for potential field data and a detailed comparison about similarities and differences among them were presented in an excellent paper by Fedi and Pilkington (2012). They showed that a proper selection of the depth weighting functions is critical for correct location of the sources. For example, in a case of the DEXP method, the weights are source sensitive and defined depending on the type of the sources considered. In other words, in order to optimize the weights, the DEXP method requires some *a priori* information about the source (e.g. line-mass or fault models, as discussed in Fedi and Pilkington, 2012). The migration imaging does not have this limitation because the weights are determined by the integrated sensitivity of the field, which is independent on the type of the specific source. At the same time, a limitation of migration transformation is related to the fact that, in a general case, the gravity data generated by the migration image do not fit the observed data well. In addition, for some models, as shown by Fedi and Pilkington (2012), one migration transformation

would not produce a good image. That is why, in order to produce a correct image of the source, one should apply the migration iteratively, which is the subject of our paper.

By analogy to iterative electromagnetic migration (Mehanee and Zhdanov, 2002; Ueda and Zhdanov, 2008; Zhdanov, 2002), Wan and Zhdanov (2013) introduced a method of iterative migration of the full-tensor gradient (FTG) data with a smooth stabilizer to obtain a more accurate subsurface 3D density distribution. This method is generally equivalent to regularized inversion. Traditional one-step migration or iterative migration based on the smooth stabilizer functional has disadvantages, however, especially in delineating abruptly changing structural boundaries of geological formations. In this situation, it is important to develop an alternative approach that can yield stable solutions while honouring sharp petrophysical boundaries (Zhdanov *et al.*, 2004; Zhdanov, 2015).

In this paper, we outline the basic principles of 3D iterative gravity migration and present a new approach to obtaining images with sharp boundaries based on potential field iterative migration.

## 2 MIGRATION OF GRAVITY AND GRAVITY TENSOR FIELDS AND 3D DENSITY IMAGING

The gravity field can be expressed using the following integral representation:

$$g_{\alpha}(\mathbf{r}) = A_{\alpha}(\rho) = \gamma \int \int \int_D \frac{\rho(\mathbf{r}')}{|\mathbf{r}' - \mathbf{r}|^3} K_{\alpha}(\mathbf{r}' - \mathbf{r}) dv', \quad r \notin D, \quad (1)$$

where  $g_{\alpha}(\mathbf{r})$ ,  $\alpha = x, y, z$ , are the calculated gravity responses for different components of the gravity field on the observation surface;  $\gamma$  is the gravitational constant ( $\gamma = 6.67384 \times 10^{-11} \text{m}^3/\text{kg} \times \text{s}^2$ );  $\rho$  represents the density distribution within some anomalous domain,  $D$ , in the subsurface; and  $A_{\alpha}$  are the corresponding linear operators of forward modelling. The kernels  $K_{\alpha}(\mathbf{r}' - \mathbf{r})$  are defined as follows:

$$K_{\alpha}(\mathbf{r}' - \mathbf{r}) = \alpha' - \alpha, \quad \alpha = x, y, z. \quad (2)$$

In a similar way, the forward modelling of the gravity tensor field can be expressed as follows:

$$g_{\alpha\beta}(\mathbf{r}) = A_{\alpha\beta}(\rho) = \gamma \int \int \int_D \frac{\rho(\mathbf{r}')}{|\mathbf{r}' - \mathbf{r}|^3} K_{\alpha\beta}(\mathbf{r}' - \mathbf{r}) dv', \quad r \notin D, \quad (3)$$

where  $g_{\alpha\beta}(\mathbf{r})$ ,  $\alpha, \beta = x, y, z$ , are the calculated gravity tensor field responses and  $A_{\alpha\beta}(\rho)$  are the linear operators of the

gravity tensor field. The kernels,  $K_{\alpha\beta}(\mathbf{r}' - \mathbf{r})$ , are defined as follows:

$$K_{\alpha\beta}(\mathbf{r}' - \mathbf{r}) = \begin{cases} 3 \frac{(\alpha - \alpha')(\beta - \beta')}{|\mathbf{r}' - \mathbf{r}|^2}, & \alpha \neq \beta \\ 3 \frac{(\alpha - \alpha')^2}{|\mathbf{r}' - \mathbf{r}|^2} - 1, & \alpha = \beta \end{cases}, \quad \alpha, \beta = x, y, z. \quad (4)$$

In addition to the gravity tensor components described by equations (3) and (4), the gravity gradiometers also measure the difference between the gradients:

$$g_{\Delta}(\mathbf{r}) = 1/2 (g_{xx} - g_{yy}). \quad (5)$$

This difference can be calculated as follows:

$$g_{\Delta}(\mathbf{r}) = A_{\Delta}(\rho) = \gamma \int \int_D \frac{\rho(\mathbf{r}')}{|\mathbf{r}' - \mathbf{r}|^3} K_{\Delta}(\mathbf{r}' - \mathbf{r}) d\mathbf{v}', \quad \mathbf{r} \notin D, \quad (6)$$

where

$$K_{\Delta}(\mathbf{r}' - \mathbf{r}) = \frac{3(x' - x)^2 - (y' - y)^2}{2|\mathbf{r}' - \mathbf{r}|^2}. \quad (7)$$

Following Zhdanov (2002) and Zhdanov *et al.* (2011), the *migration gravity field*,  $g_{\alpha}^m(\mathbf{r})$ , is presented as a result of application of the adjoint gravity operator,  $A_{\alpha}^*$ , to the observed components of the gravity field:

$$g_{\alpha}^m(\mathbf{r}) = A_{\alpha}^* g_{\alpha}, \quad (8)$$

where the adjoint operator,  $A^*$ , for the gravity migration problem is given by the following integral (Zhdanov *et al.*, 2011; Zhdanov, 2015):

$$A_{\alpha}^*(f) = \gamma \int \int_S \frac{f(\mathbf{r})}{|\mathbf{r}' - \mathbf{r}|^3} K_{\alpha}(\mathbf{r}' - \mathbf{r}) d\mathbf{s}. \quad (9)$$

In a similar way, the *migration gravity tensor fields*,  $g_{\alpha\beta}^m$  and  $g_{\Delta}^m$ , have the following expressions, respectively:

$$g_{\alpha\beta}^m(\mathbf{r}) = A_{\alpha\beta}^* g_{\alpha\beta}, \quad (10)$$

$$g_{\Delta}^m(\mathbf{r}) = A_{\Delta}^* g_{\Delta}, \quad (11)$$

where the adjoint operators for gravity gradients are defined by the following formula (Zhdanov *et al.*, 2011; Zhdanov, 2015):

$$A_{\alpha\beta}^*(f) = \gamma \int \int_S \frac{f(\mathbf{r})}{|\mathbf{r}' - \mathbf{r}|^3} K_{\alpha\beta}(\mathbf{r}' - \mathbf{r}) d\mathbf{s}, \quad (12)$$

$$A_{\Delta}^*(f) = \gamma \int \int_S \frac{f(\mathbf{r})}{|\mathbf{r}' - \mathbf{r}|^3} K_{\Delta}(\mathbf{r}' - \mathbf{r}) d\mathbf{s}. \quad (13)$$

From a physical point of view, the migration field can be presented as the gravity field of the virtual sources, which are the mirror images of the true sources with respect to the observational surface. Nevertheless, the migrated gravity fields retain information about the initial density distribution in the lower half-space, which highlights why they can be used in imaging of the sources of the gravity field.

Since the migrated field is inversely proportional to the square (for gravity field components) or cube (for gravity tensor components) of the depth (equations (9), (12) and (13)), a correct depth distribution of the density anomaly cannot be provided directly from the migration of the observed gravity data. It is necessary to apply a suitable depth-weighting function to the migrated gravity fields to determine the correct locations of their sources. To obtain an appropriate weighting operator, the integrated sensitivity,  $S_{\alpha} = \|\delta g_{\alpha}\|_D / |\delta \rho|$  of the data to the density has to be used (Zhdanov, 2015).

As a result, the migration density is defined as follows:

$$\rho_{\alpha}^m(\mathbf{r}) = k_{\alpha} (W_m^* W_m)^{-1} A_{\alpha}^* g_{\alpha} = k_{\alpha} w_{\alpha}^{-2}(z) g_{\alpha}^m(\mathbf{r}), \quad (14)$$

where  $k_{\alpha}$  can be obtained using a linear line search:

$$k_{\alpha} = \frac{\|A_{\alpha}^{w*} g_{\alpha}\|_M^2}{\|A_{\alpha}^w A_{\alpha}^{w*} g_{\alpha}\|_D^2}, \quad (15)$$

$$A_{\alpha}^w = A_{\alpha} W_{\alpha}^{-1}, \quad (16)$$

and  $W_m = W_{\alpha}$ ,  $\alpha = x, y, z$ , is the weighting operator of multiplication of the density  $\rho$  by a function  $w_{\alpha}$  defined for the corresponding components of the gravity field,  $g_{\alpha}$ , as follows:

$$w_{\alpha} = \sqrt{S_{\alpha}}, \quad \alpha = x, y, z. \quad (17)$$

In the last formula,  $S_{\alpha}$  denotes the integrated sensitivity which can be calculated by the following formula:

$$S_{\alpha} = c_{\alpha} \frac{1}{|z|}, \quad z < 0, \quad \alpha = x, y, z, \quad (18)$$

where  $c_\alpha$  are the corresponding constants for different components of the gravity field equal to

$$c_x = c_y = \gamma \sqrt{\frac{\pi}{2}}, \quad c_z = \gamma \sqrt{\pi}. \quad (19)$$

Using equations (17), (18) and (19), migration density,  $\rho_\alpha^m(\mathbf{r})$ , defined by equation (14), can be rewritten as follows:

$$\rho_\alpha^m(\mathbf{r}) = \frac{k_\alpha}{c_\alpha} |z| g_\alpha^m(\mathbf{r}). \quad (20)$$

Thus, the migration transformation with the depth weighting provides a stable algorithm for calculating migration density. We should emphasize that the depth weighting in migration imaging does not depend on the source property, which is the case, for example, in other fast imaging methods, such as the DEXP method (Fedi and Pilkington, 2012). That is why in order to produce a correct image of the source one should apply the migration iteratively, as discussed in the next sections.

In a similar way, the tensor field migration density can be expressed as follows:

$$\rho_{\alpha\beta}^m(\mathbf{r}) = k_{\alpha\beta} (W_m^* W_m)^{-1} A_{\alpha\beta}^* g_{\alpha\beta} = k_{\alpha\beta} w_{\alpha\beta}^{-2}(z) g_{\alpha\beta}^m(\mathbf{r}), \quad (21)$$

$$\rho_\Delta^m(\mathbf{r}) = k_\Delta (W_m^* W_m)^{-1} A_\Delta^* g_\Delta = k_\Delta w_\Delta^{-2}(z) g_\Delta^m(\mathbf{r}), \quad (22)$$

where

$$k_{\alpha\beta} = \frac{\|A_{\alpha\beta}^{w*} g_{\alpha\beta}\|_M^2}{\|A_{\alpha\beta}^w A_{\alpha\beta}^{w*} g_{\alpha\beta}\|_D^2}, \quad k_\Delta = \frac{\|A_\Delta^{w*} g_\Delta\|_M^2}{\|A_\Delta^w A_\Delta^{w*} g_\Delta\|_D^2}, \quad (23)$$

and functions  $w_{\alpha\beta}$  and  $w_\Delta$  represent the weighting operators, respectively:

$$w_{\alpha\beta} = \sqrt{S_{\alpha\beta}}, \quad w_\Delta = \sqrt{S_\Delta}. \quad (24)$$

The integrated sensitivity of the gravity tensor field is calculated using the following formulas:

$$S_{\alpha\beta} = c_{\alpha\beta} \frac{1}{z^2}, \quad S_\Delta = c_\Delta \frac{1}{z^2}, \quad \alpha, \beta = x, y, z, \quad (25)$$

where  $c_{\alpha\beta}$  and  $c_\Delta$  are the corresponding constants for different components equal to

$$c_{zz} = c_{zx} = c_{zy} = \Upsilon \frac{\sqrt{3\pi}}{2}, \quad c_{xx} = c_{yy} = c_{xy} = c_\Delta = \Upsilon \frac{3\sqrt{\pi}}{4}. \quad (26)$$

Substituting equations (24) and (25) for the weighting function,  $w_{\alpha\beta}$ , back into equations (21) and (22), we obtain

$$\rho_{\alpha\beta}^m(\mathbf{r}) = \frac{k_{\alpha\beta}}{c_{\alpha\beta}} z^2 g_{\alpha\beta}^m(\mathbf{r}), \quad \rho_\Delta^m(\mathbf{r}) = \frac{k_\Delta}{c_\Delta} z^2 g_\Delta^m(\mathbf{r}). \quad (27)$$

### 3 ITERATIVE GRAVITY MIGRATION WITH FOCUSING STABILIZER

Zhdanov (2002, 2011) introduced a rapid imaging of the density distribution in the lower half-space, based on migration transformation. The migration images, however, do not resolve well the boundaries of the density anomalies due to the diffusive nature of the potential fields and migration itself. A better-quality migration image could be produced by repeating the migration process iteratively using the conjugate gradient method (Wan and Zhdanov, 2013; Zhdanov *et al.*, 2020).

For example, at the second iteration, we apply the migration to the gravity tensor residual field,  $[g_{\alpha\beta}^{\text{pred}}(\mathbf{r}) - g_{\alpha\beta}^{\text{obs}}(\mathbf{r})]$ , (where subscripts ‘obs’ and ‘pred’ correspond to the observed data and numerically simulated data for the migration density model, respectively) and produce the density variation,  $\delta\rho_1$ , of the first migration density model ( $\rho_1$ ) generated by the same transformation. By adding  $\delta\rho_1$ , we arrive at the second iteration of the migration density model:

$$\rho_2 = \rho_1 + \delta\rho_1 = \rho_1 - k_1^{\alpha\beta} (W_m^* W_m)^{-1} l_1^m, \quad (28)$$

where  $k_1^{\alpha\beta}$  is step length, and  $l_1^m$  is the steepest ascent direction at the first iteration:

$$l_1^m(\rho) = A_{\alpha\beta}^* [-g_{\alpha\beta}^{\text{obs}}(\mathbf{r})], \quad (29)$$

and  $W_m$  is the weighting operator of multiplication of the density  $\rho$  by spatial weighting functions  $w_{\alpha\beta}$  and  $w_\Delta$  defined by equations (24) and (25).

A general scheme of the iterative migration can be described as follows:

$$\rho_{n+1} = \rho_n + \delta\rho_n = \rho_n - k_n^{\alpha\beta} (W_m^* W_m)^{-1} l_n^m. \quad (30)$$

where  $k_n^{\alpha\beta}$  is the step length, and  $l_n^m$  is the steepest ascent direction at the  $n$ th iteration, defined as follows:  $l_n^m(\rho) = A_{\alpha\beta}^* [g_{\alpha\beta}^{\text{pred}}(\mathbf{r}) - g_{\alpha\beta}^{\text{obs}}(\mathbf{r})]$ .

The iterative migration is terminated when the normalized misfit,  $e^2$ , between the observed and predicted data is less than or equal to the level of the noise,  $\delta^2$ , in the data:

$$e^2 = \frac{\varphi}{\|g_{\alpha\beta}^{\text{obs}}\|_D^2} \leq \delta^2, \quad (31)$$

where  $\varphi$  is a misfit functional,  $\varphi = \|g_{\alpha\beta}^{\text{pred}} - g_{\alpha\beta}^{\text{obs}}\|_D^2$ .

This new approach, as an alternative solution of the inverse problem, is similar to the algorithm of basic regularized steepest descent inversion. In a similar way, iterative migration could also be implemented in the framework of the conjugate gradient method. The density perturbation updated by migration on each iteration depends on the application of the adjoint operator to the corresponding gravity or gravity gradient residual field. This procedure, as demonstrated by Zhdanov *et al.* (2011), is essentially a *depth-weighted upward analytical continuation* of the potential field generated by the sources located in the lower half-space. The last transformation is well developed in potential field theory. In other words, iterative migration makes it possible to use the powerful and stable technique of upward continuation as a key step in the solution of the inverse problem.

Similar to inversion, iterative migration can be implemented with regularization (Zhdanov, 2015), which allows an application of both the smooth and focusing stabilizers,  $s$ . In this case, equation (30) can be rewritten as follows:

$$\rho_{n+1} = \rho_n + \delta\rho_n = \rho_n - k_n^{\alpha\beta} (W_m^* W_m)^{-1} \tilde{I}_n^{m\lambda}, \quad (32)$$

where

$$\tilde{I}_n^{m\lambda} = I_n^{m\lambda} + \beta_n^\lambda \tilde{I}_{n-1}^{m\lambda}, \quad \tilde{I}_0^{m\lambda} = I_0^{m\lambda}, \quad (33)$$

$$\beta_n^\lambda = \frac{\|I_n^{m\lambda}\|^2}{\|I_{n-1}^{m\lambda}\|^2}.$$

In the last formulas,  $\lambda$  is the optimal regularization parameter;  $I_n^{m\lambda}$  is the regularized direction of steepest descent on the  $n$ th iteration. The principles for selecting the regularization parameter,  $\lambda$ , are exactly the same as in a case of regularized inversion and involve an adaptive decrease of the regularization parameter with the iteration number (Zhdanov, 2002, 2015). On the first iteration of migration, the regularization parameter is set to zero,  $\lambda_1 = 0$ . On the second iteration, the regularization parameter is selected by balancing the values of the misfit functional,  $\varphi(\rho_1)$ , and the stabilizing functional,  $s(\rho_1)$ , computed for the migration image,  $\rho_1$  produce on the first iteration,  $\lambda_2 = \varphi(\rho_1)/s(\rho_1)$ . On the following iterations, the values of  $\lambda_{n+1}$  decrease according to a geometrical progression, as  $\lambda_{n+1} = q \lambda_n$ , where  $q < 1$ .

In the case of a smooth stabilizer, the regularized gradient direction,  $I_n^{m\lambda}$ , can be calculated by the following formula:

$$I_n^{m\lambda} = I_n^m + \lambda (\rho_n - \rho_{apr}), \quad (34)$$

where the direction of steepest ascent,  $I_n^m$ , is computed based on migration of the corresponding gravity tensor residual field

component:

$$\begin{aligned} I_n^m &= I_{\alpha\beta}^m(\rho) = \gamma \int \int_S \frac{g_{\alpha\beta}(\mathbf{r}) - g_{\alpha\beta}^{\text{obs}}(\mathbf{r})}{|\mathbf{r}' - \mathbf{r}|^3} K_{\alpha\beta}(\mathbf{r}' - \mathbf{r}) ds \\ &= A_{\alpha\beta}^* [g_{\alpha\beta}(\mathbf{r}) - g_{\alpha\beta}^{\text{obs}}(\mathbf{r})]. \end{aligned} \quad (35)$$

In the case of the focusing stabilizer, equation (34) is modified as follows:

$$I_n^{m\lambda} = I_n^m + \lambda W_e (\rho_n - \rho_{apr}). \quad (36)$$

Here,  $\rho_{apr}$  is a *priori* selected model of the density distribution (it can be equal to zero if no *priori* model is available);  $W_e$  is a diagonal focusing matrix (Portniaguine and Zhdanov, 1999):

$$W_e = \text{diag}((\rho_n - \rho_{apr})^2 + \varepsilon^2)^{-\frac{1}{2}}; \quad (37)$$

and  $\varepsilon$  is a focusing parameter (a small positive number), which controls the degree of focusing (Zhdanov, 2015).

The determination of the step length,  $k_n$ , is based on the optimization of the parametric functional  $P_\lambda(k_n)$  (Mehanee and Zhdanov, 2002):

$$\begin{aligned} P_\lambda(k_n) &= P_\lambda(\rho_n - k_n^{\alpha\beta} \tilde{I}_n^{m\lambda}(\rho_n)) = (A_{\alpha\beta}(\rho_n - k_n^{\alpha\beta} \tilde{I}_n^{m\lambda}) - g_{\alpha\beta})^T \\ &\quad W_d^2 (A_{\alpha\beta}(\rho_n - k_n^{\alpha\beta} \tilde{I}_n^{m\lambda}) - g_{\alpha\beta}) \\ &\quad + \lambda (\rho_n - k_n^{\alpha\beta} \tilde{I}_n^{m\lambda} - \rho_{apr})^T W_m^2 (\rho_n - k_n^{\alpha\beta} \tilde{I}_n^{m\lambda} - \rho_{apr}) \\ &= \min, \end{aligned} \quad (38)$$

where  $W_d^2$  and  $W_m^2$  are the weighting matrices of the data and model parameters (Zhdanov, 2015).

The above functional can be replaced by the second-order polynomial with respect to  $k_n^m$ . Solving the minimization problem with respect to  $k_n^{\alpha\beta}$ , we find

$$k_n^{\alpha\beta} = e \frac{R_n e [R_n^T W_d^2 (R_n - R_{n+1}(e))] + \lambda e (\tilde{I}_n^{m\lambda})^T W_m^2 (\rho_n - \rho_{apr})}{(R_n - R_{n+1}(e))^T W_d^2 (R_n - R_{n+1}(e)) + \lambda e^2 (\tilde{I}_n^{m\lambda})^T W_m^2 I_n} \quad (39)$$

and

$$R_n = A_{\alpha\beta}(\rho_n) - g_{\alpha\beta}, \quad (40)$$

$$R_{n+1}(e) = A_{\alpha\beta}(\rho_n - e \tilde{I}_n^{m\lambda}) - g_{\alpha\beta}. \quad (41)$$

where  $e \ll 1$  is a small positive number.

In a similar way, we can construct the algorithm of regularized focusing migration of the gravity tensor field. The

corresponding formulas can be obtained by a direct substitution of the forward and adjoint operators of the gravity tensor field for the corresponding operators of the gravity field in equations (32) through (41). The process of iterative migration is repeated until the normalized misfit,  $e$ , between the observed and predicted data, reaches the pre-assigned level.

We should note in the conclusion of this section that, in the framework of iterative migration, it is also possible to transfer the original model into logarithmic space to ensure that the corresponding parameters remain within reasonable boundaries, as it is done in conventional inversion (e.g. Zhdanov, 2015). However, the results presented in this paper were produced without this transformation.

#### 4 MODEL STUDY

We have examined the effectiveness of the iterative migration using synthetic gravity gradiometry data computed for a simple model, shown in Fig. 1. For testing the algorithm, the ‘observed data’,  $g_{xx}$ ,  $g_{xz}$  and  $g_{zz}$ , generated for this model, were contaminated by 5% random noise. The model consists of two rectangular bodies with the sides of 200, 400 and 200 m in the

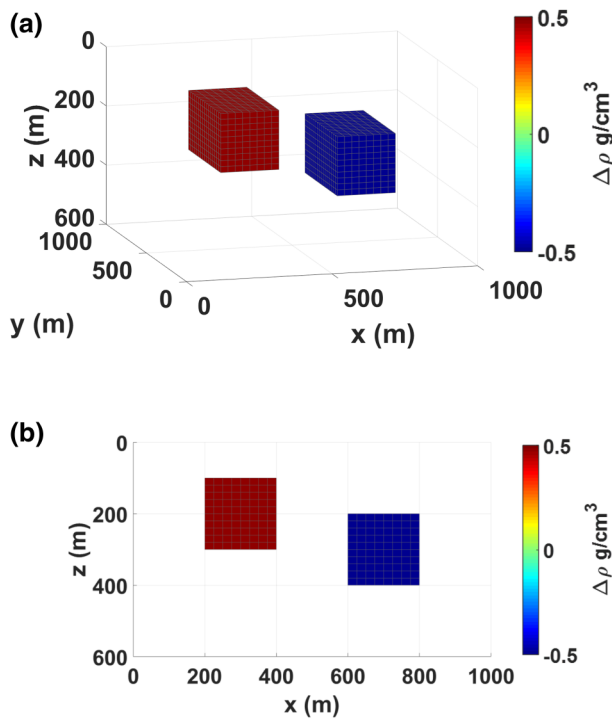


Figure 1 The synthetic model: (a) 3D view of the density model and (b) X–Z section view of the density model along the  $Y = 500$  m profile.

$x$ ,  $y$  and  $z$  directions, respectively. The top surface of one body is at a depth of 100 m, while the top surface of another body is at a depth of 200 m below the ground surface. The upper and lower bodies have a density of 0.4 and  $-0.4$  g/cm<sup>3</sup>, respectively. Figure 1 shows the 3D view of the model and a vertical X–Z section ( $Y = 500$  m) across the bodies. The observation surface is a horizontal plane ( $z = 0$  m). The area of observation extends from 0 to 1000 m in the  $x$  direction and from 0 to 1500 m in the  $y$  direction, with a 20-m interval between the data points. There are  $51 \times 51 = 2061$  data points for each component of the gravity gradiometry tensor. The 3D volume of the migration domain was divided into 6400 cells ( $20 \times 20 \times 16$ ), with each cubic cell having 50 m side.

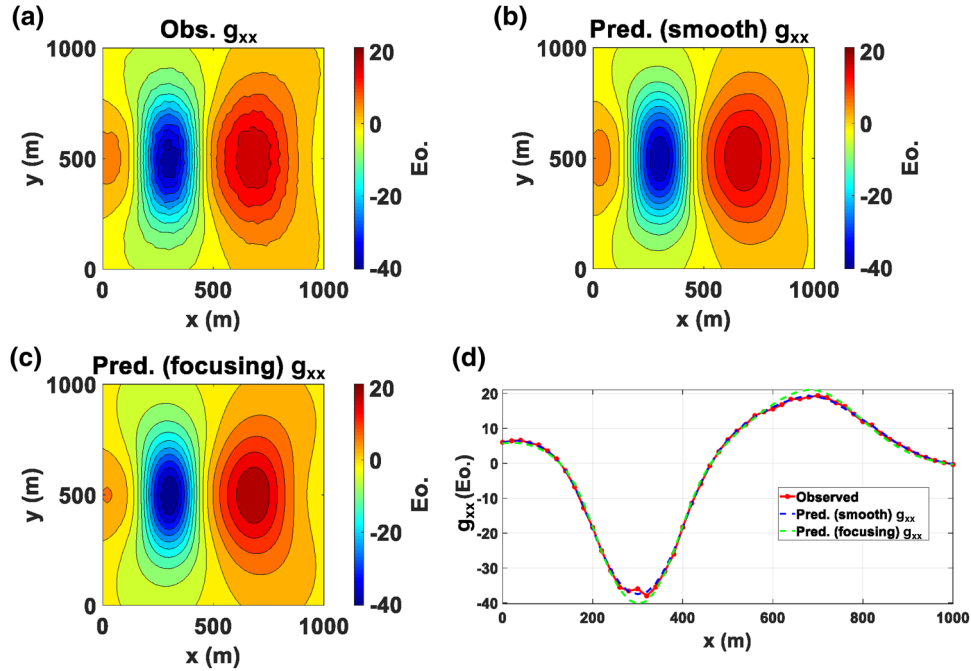
The observed and predicted data (produced by smooth and focusing migrations) of the  $g_{xx}$  component are shown in Fig. 2. The first panel from the top shows the observed field; the second panel presents the predicted field calculated from the density distribution derived by smooth iterative migration; the third panel represents the predicted field produced using focusing iterative migration; and the last panel presents a comparison between the observed and predicted data for the  $g_{xx}$  component along the profile  $y = 500$  m. One can see that the predicted field calculated using both smooth and focusing stabilized functionals matches the observed data well.

Figure 3 shows the results of iterative migration using both smooth (Fig. 3a) and focusing (Fig. 3b) stabilizers for  $g_{xx}$  component data. The iterative migration was terminated when the normalized misfit reached 5% (noise level). The black dashed lines represent the true location of the anomalous bodies. One can see that iterative focusing migration recovers a more ‘focused’ image of the target than the smooth migration.

Figure 4 presents a comparison between the predicted and observed fields for the  $g_{xz}$  component. The first panel on the top left shows the observed field; the second panel on the top right presents the predicted field calculated from the density distribution derived by smooth iterative migration; the third panel on the bottom left represents the field produced by focusing iterative migration; and the last panel presents a comparison between the observed and predicted data for the  $g_{xz}$  component along the profile  $y = 500$  m. One can see again a good fit between the predicted and observed data for both smooth and focusing migrations.

Figure 5 demonstrates the results of iterative migration using both smooth (Fig. 5a) and focusing (Fig. 5b) stabilizers for the  $g_{zz}$  component. The iterative process was terminated when the normalized misfit reached the 5% noise level.





**Figure 2** Observed and predicted  $g_{xx}$  component data. (a) Observed field, (b) predicted field derived by smooth iterative migration, (c) predicted field corresponding to focusing iterative migration and (d) comparison of the observed and predicted data for the  $g_{xx}$  component at profile  $y = 500$  m.

The true location of the bodies is shown by the black dashed squares. Compared with the results shown in Fig. 3, the iterative focusing migration based on the  $g_{xz}$  component produces a more contrast image of the density anomalies and also recovers the density of both targets close to their true value (0.4 and  $-0.4$   $g/cm^3$ ).

Baniamerian *et al.* (2016) demonstrated that one could increase the compactness of the source through weighting the model produced by the DEXP method with a compacting function. This paper develops a different algorithm based on the focusing iterative migration. The result will be simi-

lar in some cases, where the migration and DEXP method generate the same initial models. However, while the ‘compact depth from extreme points’ is still a fast imaging algorithm, focusing iterative migration represents a more general approach because it delivers a rigorous solution of the inverse problem.

Finally, we applied the iterative migration to the vertical gradient of the gravity field. Figure 6 shows a comparison between the predicted and observed  $g_{zz}$  field data. One can see that the predicted field comfortably matches the observed data under 5% data fitting.

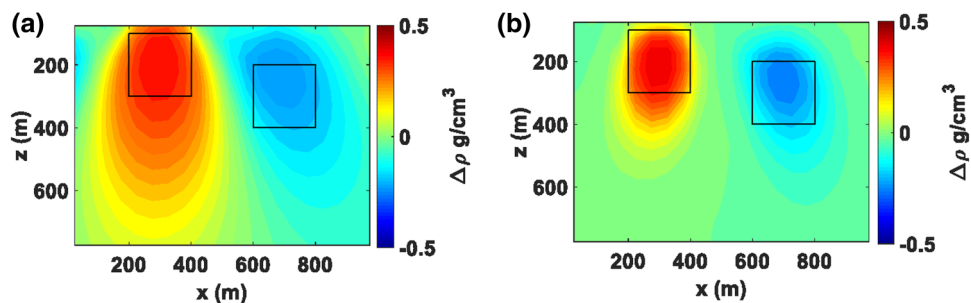


**Figure 3** The iterative migration results using  $g_{xx}$  component data. (a) X–Z section of the smooth migration density result along  $y = 500$  m and (b) X–Z section of the focusing migration density result along  $y = 500$  m.

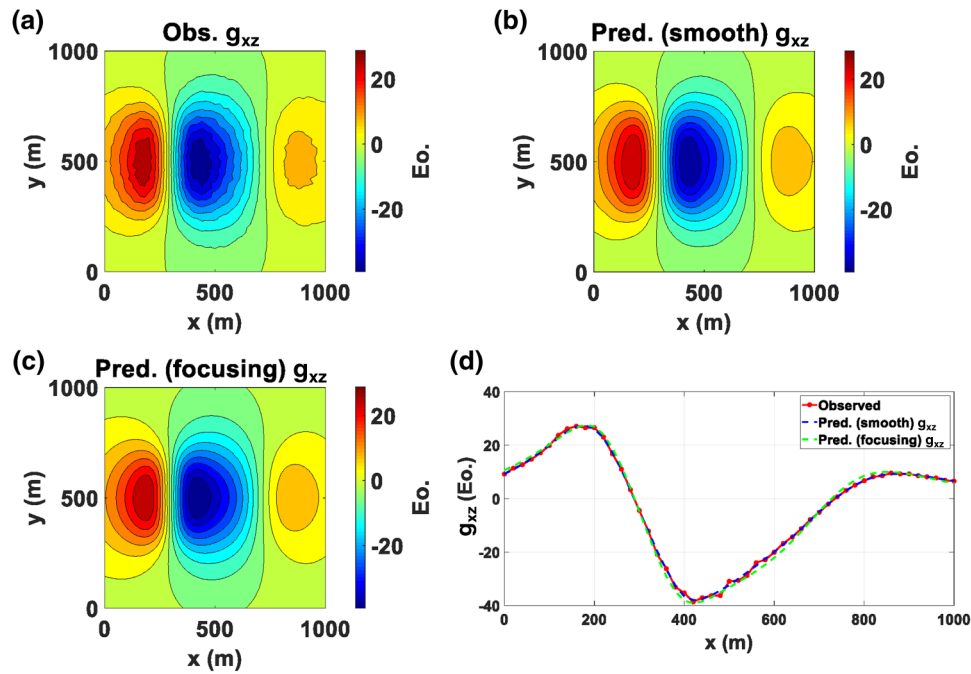


Figure 4 Observed and predicted  $g_{xz}$  component data. (a) Observed field, (b) predicted field derived by smooth iterative migration, (c) predicted field corresponding to focusing iterative migration and (d) comparison of the observed and predicted data for the  $g_{xz}$  component at profile  $y = 500$  m.

Figure 7 presents the results of iterative migration of the  $g_{zz}$  component using both smooth (Fig. 7a) and focusing (Fig. 7b) stabilizers. The true position of the bodies is represented by the dark dashed lines. The migration of the  $g_{zz}$  component delineates relatively well the boundaries of the anomalous bodies and provides an accurate estimate of the density contrast. The different components of the gravity tensor have different sensitivities to the sources. This is reflected in the migration images.

In general, the results of the synthetic study demonstrate that smoothing iterative migration generates a very diffuse image with the boundaries of the two anomalies being blurred

and hard to distinguish. Using focusing iterative migration helps produce a more focused image which captures the spatial position of the anomalous bodies and provides a reasonable estimate of the density contrast

### 5 CASE STUDY: MIGRATION OF FULL-TENSOR GRADIENT DATA COLLECTED IN THE NORDKAPP BASIN

The Nordkapp Basin is a deep, narrow salt basin in the southern Barents Sea shown in Fig. 8, which also depicts the main structural elements in the target area. The southwestern part

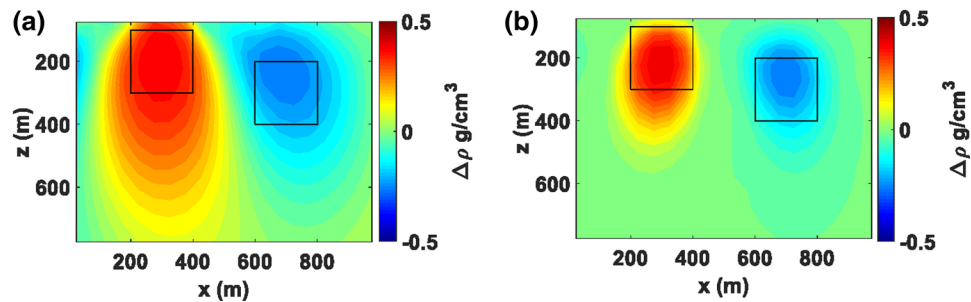


Figure 5 The iterative migration results using  $g_{xz}$  component data. (a) X-Z section of the smooth migration density result along  $y = 500$  m and (b) X-Z section of the focusing migration density result along  $y = 500$  m.



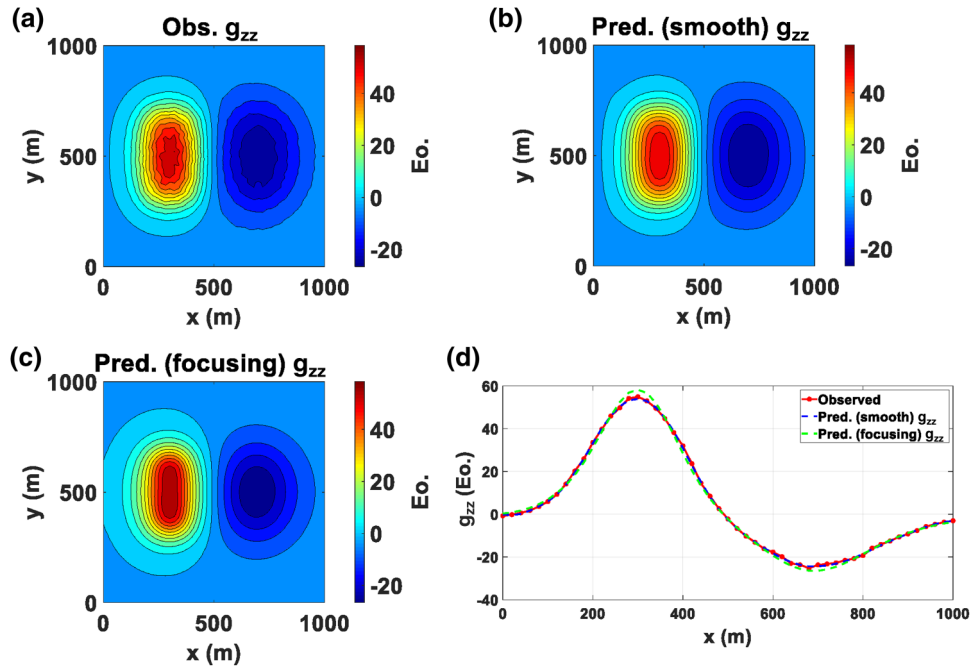


Figure 6 Observed and predicted  $g_{zz}$  component data. (a) Observed field, (b) predicted field derived by smooth iterative migration, (c) predicted field corresponding to focusing iterative migration and (d) comparison of the observed and predicted data for the  $g_{zz}$  component at profile  $y = 500$  m.

of the Nordkapp Basin (the Obelix survey location) is a narrow, northeast-oriented sub-basin approximately 150 km long and 25–50 km wide. It contains 17 salt diapirs located along its axis (Fig. 9). The northeastern part of the basin is a wider east-oriented sub-basin approximately 200 km long and 50–70 km wide. More than 16 salt diapirs occur west of the  $32^\circ$  E meridian line. Exploration in the Nordkapp Basin started in the 1980s but remained relatively limited until the early 1990s. Recent improvements in the interpretation of the basin's structural history and discovery of hydrocarbons in wells outside

the basin suggest that it is a promising target for further exploration.

Figure 9 also depicts the main structural elements in the target area and the full-tensor gradient (FTG) survey location. The predominant exploration characteristics of this area are the complexity of the salt diapirs and their associated geological structural traps. With improvements in the quality of seismic methodologies and structural interpretation, the mapping of hypothesized salt structures in the Nordkapp Basin has advanced from broad salt stocks with vertical flanks to

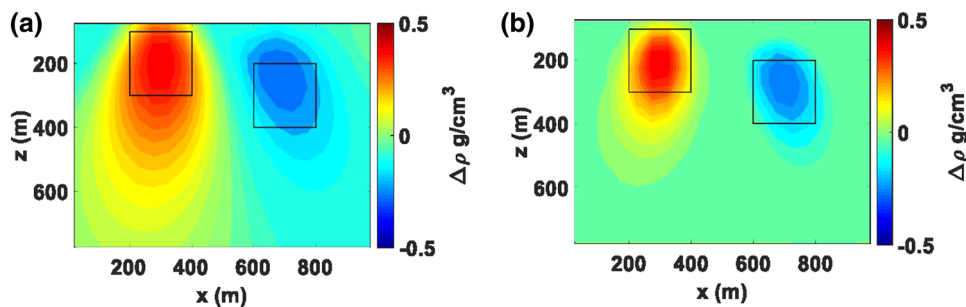


Figure 7 The iterative migration results using  $g_{zz}$  component data. (a) X–Z section of the smooth migration density result along  $y = 500$  m and (b) X–Z section of the focusing migration density result along  $y = 500$  m.

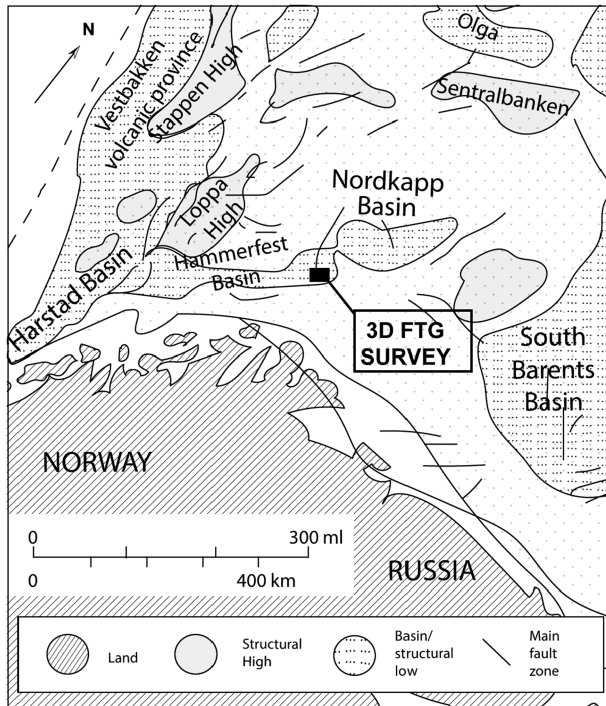


Figure 8 Main structural elements in the Barents Sea area showing the location of the Nordkapp Basin and the 3D FTG survey. Modified from Nilsen *et al.* (1995).

geometries with increasing complexity with wide diapir angles over narrow stems (Koyi *et al.*, 1993a; Henriksen and Voren, 1996; Bugge *et al.*, 2002; Gernigon *et al.*, 2011; Stadler *et al.*, 2014; Mattos *et al.*, 2016; George *et al.*, 2017; Koehl *et al.*, 2018; Rojo and Escalona, 2018; Rojo *et al.*, 2019). The uncertainty and exploitation risk in the area result from intense seismic imaging distortion due to these salt features (essentially the challenge of mapping the salt base using seismic methods).

In 2008, a 3D ship-borne FTG survey was acquired in the area shown in Fig. 9 with line spacing of 25 m and the inline sample spacing of 25 m by Bell Geospace on behalf of StatoilHydro. The gravity corrections, including instrument drift, tidal correction, theoretical gravity correction, free air correction, terrain correction and isostatic correction were applied to the FTG data, and the observation surface was shifted down to the horizontal datum below bathymetry after correction.

The expectation was that the FTG data would provide a means both to successfully evaluate the complex salt overhang geometries (defining the salt base, flank and salt base) and to improve the seismic imaging process (via Prestack Depth Mi-

gration and PSDM methods). The FTG anomalies, by their very nature, could help to identify, map and examine the geometries and edges of salt dome which plays a vital role in the comprehensive geological interpretation. The density range of the base Tertiary rocks in the study area is approximately 2.30–2.38 g/cm<sup>3</sup> (Koyi *et al.*, 1993b), and the salt diapirs are normally manifested by density anomalies with negative values (around –0.2 to –0.4 g/cm<sup>3</sup>) (Zhdanov *et al.*, 2010).

The purpose of the FTG survey was to produce extra information for the assessment of these complex salt overhang structures. FTG is an intrinsically suitable solution to such problems, being highly sensitive to detect geological anomalies with significant density contrasts.

A 3D inversion was implemented for the FTG data by Wan and Zhdanov (2008), who described the results of inversion using the focusing regularization. The goal of our study is to image the geometry of salt diapirs G2 and F2 by using focusing iterative migration of the FTG survey data. In order to achieve the computational efficiency while producing correct imaging of the subsurface density distribution, the gravity tensor component  $g_{zz}$  was selected for the migration analysis. The map of the observed data set is given in Fig. 10(a). There is a profile A-A' running across the salt diapir G2. Profile S-S' shows the location of the seismic section across the salt diapir F2. The seismic depth migration section along S-S' is mainly used for further validation of the migration results. The migration modelling domain had the size of 20 km (east–west) × 10 km (north–south) and a depth of 8 km. The volume of migration domain was discretized into 50 × 28 × 32 = 44,809 cells, where the size of the cells was 400 m × 400 m × 250 m.

Wan and Zhdanov (2008) applied the regularized focusing 3D inversion to the same FTG data which made it possible to make a comparison with the migration results. The inversion modelling domain had the size of 28 km (east–west) × 17 km (north–south) and a depth of 8 km. The volume of inversion domain was discretized into 281 × 171 × 59 = 2,835,009 cells, with the cell size equal to 100 m × 100 m × 100 m.

A sufficient number of migration iterations were carried out such that the normalized misfit between the observed and predicted data reached the noise level (below 5%). Figure 10 shows a comparison between the observed (upper panel) and predicted (lower panel)  $g_{zz}$  data produced by iterative migration. One can see a very good data fitting corresponding to a misfit of 5%. Figure 11 presents vertical sections along

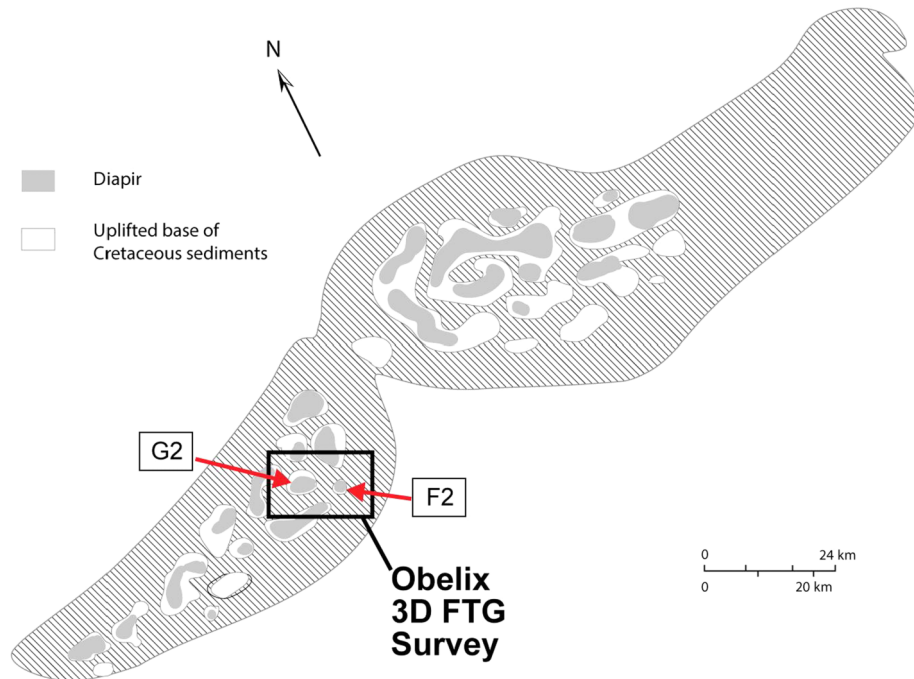


Figure 9 Simplified structural map of the Nordkapp Basin showing the salt diapirs and the main fault zones. Black areas indicate sub-crops of diapirs at or near Pliocene–Pleistocene unconformity. Modified from Nilsen *et al.* (1995).

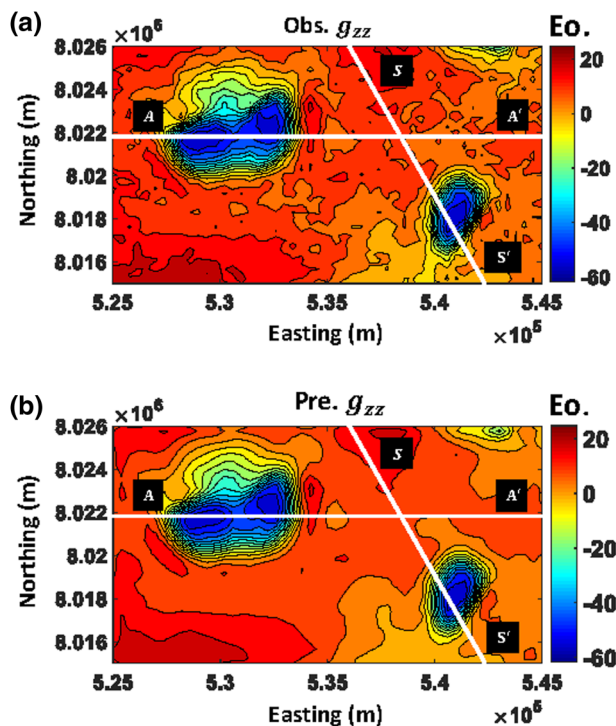


Figure 10 Maps of the observed (top panel) and predicted (bottom panel)  $g_{zz}$  component of the full-tensor gradiometry (FTG), produced by iterative migration.

profile A-A' and horizontal slices of recovered density produced by focusing migration and inversion, respectively. Figure 11(a) shows the observed data (solid red line) in comparison with the predicted data (dashed green line) along the profile. Figure 11(b) presents the vertical section of the density contrast produced by the focusing iterative migration, and Fig. 11(c) shows the same density section generated by regularized inversion. For comparison, one can see that the shape of the salt diapir is consistent in both images. Figure 11(d,e) shows two horizontal slices of the migrated and inverted density contrast at a depth of  $z = 3000$  m. It demonstrates a similarity in shape of both results.

Figure 12 shows a seismic depth migration section along the profile S-S' running across one of salt diapir F2, which outlines its horizontal extent very well; however, one can observe some distortions around the salt diapir area due to strong free-surface and internal multiples and large acoustic impedance contrast between the salt diapirs and host rock (Wan and Zhdanov, 2008). Figure 13 presents the density cross section superimposed on the seismic depth migration image along the profile S-S'. Unfortunately, seismically interpreted salt outline was not available for this diapir structure. However, a visual qualitative comparison shows that the top of salt is clearly identified in the density model and both flanks of the salt

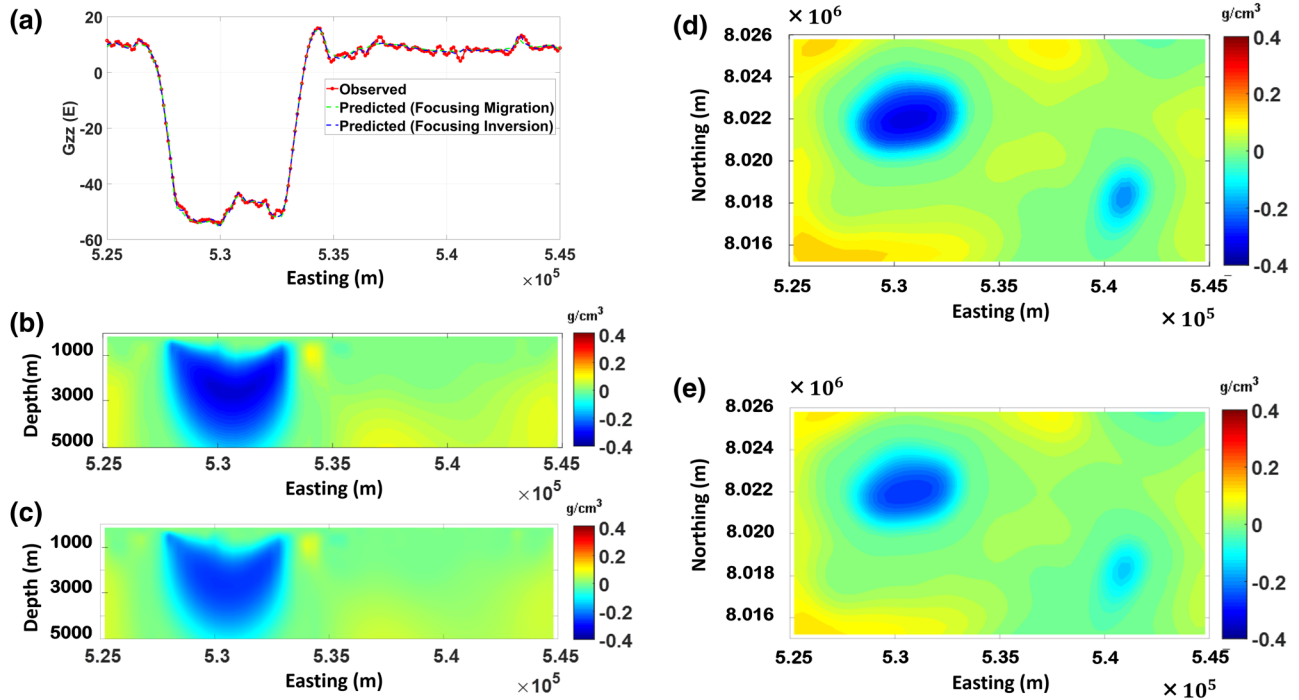


Figure 11 The vertical sections along profile A-A' and horizontal slices at a depth of  $z = 3000$  m of the density models produced by focusing migration and inversion, respectively. (a) Plots of the observed (red line) and predicted data for the results of migration (green line) and rigorous inversion (dashed black line) along profile A-A'. (b,d) Vertical and horizontal sections, respectively, of the density model produced by focusing migration, (c,e) similar sections of the inverse model produced by the focusing inversion.

diapir are, apparently, in good agreement with seismic image. Moreover, the density distribution produced by focusing migration helps define the geometry of the salt diapir F2 on the flanks more clearly than the seismic migration image.

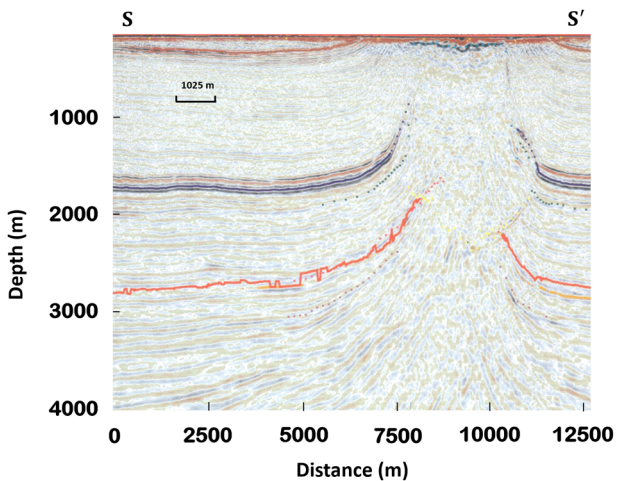


Figure 12 A seismic depth migration section S-S' from seismic survey running across salt diapir F2.

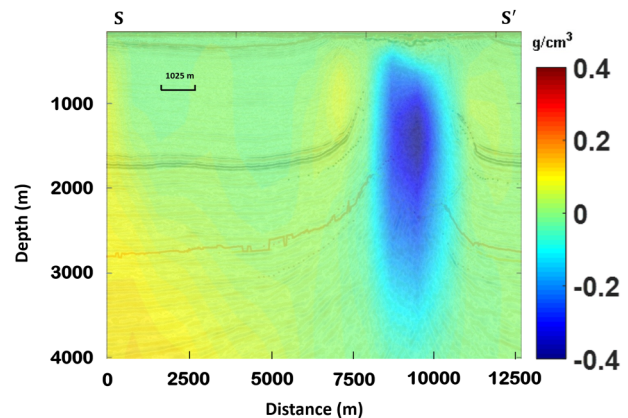


Figure 13 The density cross section produced by gravity gradient migration superimposed on the seismic depth migration image along profile S-S', shown in Fig. 10.

## 6 CONCLUSIONS

The migration of potential field involves a direct integral transformation of the gravity field and/or gradients, so that an approximate 3D density distribution can be obtained. Iterative migration is the practical equivalent to the gradient-type



inversion algorithm but with one fundamental difference – the density perturbation on each iteration can be determined through the migration of the corresponding gravity or gravity gradient residual field data. This has important significance as the last transformation has a clear physical interpretation. Specifically, iterative migration is based on the repeated ‘upward continuations’ of the residual fields (actually directed downward but away from the mirror sources of the field), which is the stable and well-established transformation of the potential fields.

Our numerical modelling and migration results show that focusing iterative migration recovers the images with sharp boundaries of the density anomalies and also provides a good estimate of the density contrast which is difficult to achieve using the smooth migration.

We have also demonstrated that focusing gravity migration could be considered an effective technique for identifying sea-bottom salt diapir structures using the full-tensor gradient (FTG) data. One can see that the geometry of the salt diapirs recovered by the 3D migration imaging on a coarse grid is almost equivalent to the one obtained by traditional 3D focusing inversion on a fine grid.

It is worth noting that the computational cost of the migration algorithm is lower than that of conventional inversion. Hence, migration can be used to quickly image the geological structures from the FTG data. Indeed, the results of 3D focusing iterative migration presented in this paper were produced on a personal computer with Intel Core i7 CPU running at 2.8 GHz and required less than half an hour for the case study. In contrast, the 3D focusing inversion algorithm was run for around 4 hours on the University of Utah Center for High Performance Computing’s Ember cluster which had 260 nodes, each equipped with two hexa-core Intel Xeon CPUs running at 2.8 GHz with 24 GB of RAM and QDR InfiniBand interconnect.


## ACKNOWLEDGEMENTS


We are thankful to the Consortium for Electromagnetic Modelling and Inversion, University of Utah, to the Rock Physics Lab, the University of Houston and to TechnoImaging for help with this research. This work was supported by the Russian Science Foundation, project No. 18-71-10071. We acknowledge Dr Brian Farrelly for providing the FTG data. We thank Drs Ed Biegert and Fuensanta G. Montesinos for their insightful comments and corrections which helped improve the manuscript. The synthetic data are available in the Supporting Information (SI) attachments.

## DATA AVAILABILITY STATEMENT

Due to confidential nature, we were not allowed to release the original FTG data for public domain. The synthetic data can be released with no problem. The synthetic data can be provided by the authors upon the request.

## ORCID

Zhengwei Xu  <https://orcid.org/0000-0001-9349-5724>

Michael S. Zhdanov 

<https://orcid.org/0000-0002-3862-587X>

## REFERENCES

- An, M. and Assumpção, M. (2006) Crustal and upper mantle structure in the intracratonic Paraná Basin, SE Brazil, from surface wave dispersion using genetic algorithms. *Journal of South American Earth Sciences*, 21, 173–184.
- Baniamarian, J., Fedi, M. and Oskooi, B. (2016) Research note: compact depth from extreme points: a tool for fast potential field imaging. *Geophysical Prospecting*, 64, 1386–1398.
- Berkhout, A.J. (2012) *Seismic Migration: Imaging of Acoustic Energy by Wave Field Extrapolation: Imaging of Acoustic Energy by Wave Field Extrapolation*. Elsevier, ISBN 0444602003.
- Bugge, T., Elvebak, G., Fanavoll, S., Mangerud, G., Smelror, M., Weiss, H.M. *et al.* (2002) Shallow stratigraphic drilling applied in hydrocarbon exploration of the Nordkapp Basin, Barents Sea. *Marine and Petroleum Geology*, 19, 13–37.
- Claerbout, J.F. (1985) *Imaging the Earth’s Interior*. Oxford: Blackwell Scientific Publications.
- Dransfield, M. (2010) Conforming falcon gravity and the global gravity anomaly. *Geophysical Prospecting*, 58, 469–483.
- Fedi, M. (2007) DEXP: a fast method to determine the depth and the structural index of potential fields sources. *Geophysics*, 72, I1–I11.
- Fedi, M. and Florio, G. (2006) SCALFUN: 3D analysis of potential field scaling function to determine independently or simultaneously structural index and depth to source. In: *SEG Technical Program Expanded Abstracts 2006*, pp. 963–967. Society of Exploration Geophysicists, ISBN 1052–3812.
- Fedi, M. and Pilkington, M. (2012) Understanding imaging methods for potential field data. *Geophysics*, 77, G13–G24.
- George, M., Olakunle, O.K., Emil, J.S. and Abrahamson, P. (2017) Seismic interpretation and characterization of anhydrite caprocks in the Tromso Basin, SW Barents Sea. *Marine Geology*, 390, 36–50.
- Gernigon, L., Bronner, M., Fichler, C., Lovas, L., Marelllo, L. and Olsen, O. (2011) Magnetic expression of salt diapir-related structures in the Nordkapp Basin, western Barents Sea. *Geology*, 39, 135–138.
- Hautot, S., Single, R.T., Watson, J., Harrop, N., Jerram, D.A., Tarits, P. *et al.* (2007) 3-D magnetotelluric inversion and model validation with gravity data for the investigation of flood basalts and associated volcanic rifted margins. *Geophysical Journal International*, 170, 1418–1430.

- Henriksen, S. and Vorren, T.O. (1996) Early Tertiary sedimentation and salt tectonics in the Nordkapp Basin, southern Barents Sea. *Norsk Geologisk Tidsskrift*, 76, 33–44.
- Hornby, P., Boschetti, F. and Horowitz, F.G. (1999) Analysis of potential field data in the wavelet domain. *Geophysical Journal International*, 137, 175–196.
- Işık, M. and Şenel, H. (2009) 3D gravity modeling of Büyük Menderes basin in Western Anatolia using parabolic density function. *Journal of Asian Earth Sciences*, 34, 317–325.
- Koehl, J.B.P., Bergh, S.G., Henningsen, T. and Faleide, J.I. (2018) Middle to Late Devonian-Carboniferous collapse basins on the Finnmark Platform and in the southwesternmost Nordkapp basin, SW Barents Sea. *Solid Earth*, 9, 341–372.
- Koyi, H., Talbot, C.J. and Tørudbakken, B.O. (1993a) Salt diapirs of the southwest Nordkapp Basin: analogue modelling. *Tectonophysics*, 228, 167–187.
- Koyi, H., Jenyon, M. and Petersen, K. (1993b) The effect of basement faulting on diapirism. *Journal of Petroleum Geology*, 16, 285–312.
- Li, Y. (2001) 3-D inversion of gravity gradiometer data. In: *SEG Technical Program Expanded Abstracts 2001*, pp. 1470–1473. Society of Exploration Geophysicists, ISBN 1052–3812.
- Li, Y. and Oldenburg, D.W. (1998) 3-D inversion of gravity data. *Geophysics*, 63, 109–119.
- Liu, S., Baniamerian, J. and Fedi, M. (2019) Imaging methods versus inverse methods: an option or an alternative? *IEEE Transactions on Geoscience and Remote Sensing*, 58(5), 3484–3494.
- Mammo, T. (2013) Crustal structure of the flood basalt province of Ethiopia from constrained 3-D gravity inversion. *Pure and Applied Geophysics*, 170, 2185–2206.
- Mattos, N.H., Alves, T.M. and Omosanya, K.O. (2016) Crestal fault geometries reveal late halokinesis and collapse of the Samson Dome, Northern Norway: implications for petroleum systems in the Barents Sea. *Tectonophysics*, 690, 76–96.
- Mehanee, S.A. and Zhdanov, M.S. (2002) 3-D finite difference iterative migration of the electromagnetic field. In: *SEG Technical Program Expanded Abstracts 2002*, pp. 657–660. Society of Exploration Geophysicists, ISBN 1052–3812.
- Nagihara, S. and Hall, S.A. (2001) Three-dimensional gravity inversion using simulated annealing: constraints on the diapiric roots of allochthonous salt structures. *Geophysics*, 66, 1438–1449.
- Nilsen, K.T., Vendeville, B.C. and Johansen, J.T. (1995) Influence of regional tectonics on halokinesis in the Nordkapp Basin, Barents Sea. *Salt Tectonics: A Global Perspective*, 65, 413–436.
- Portniaguine, O. and Zhdanov, M.S. (1999) Focusing geophysical inversion images. *Geophysics*, 64, 874–887.
- Ren, Z., Zhong, Y., Chen, C., Tang, J., Kalscheuer, T., Maurer, H. et al. (2018) Gravity gradient tensor of arbitrary 3D polyhedral bodies with up to third-order polynomial horizontal and vertical mass contrasts. *Surveys in Geophysics*, 39, 901–935.
- Rojo, L.A. and Escalona, A. (2018) Controls on minibasin infill in the Nordkapp Basin: evidence of complex Triassic synsedimentary deposition influenced by salt tectonics. *Aapg Bulletin*, 102, 1239–1272.
- Rojo, L.A., Cardozo, N., Escalona, A. and Koyi, H. (2019) Structural style and evolution of the Nordkapp Basin, Norwegian Barents Sea. *Aapg Bulletin*, 103, 2177–2217.
- Sailhac, P. and Gibert, D. (2003) Identification of sources of potential fields with the continuous wavelet transform: two-dimensional wavelets and multipolar approximations. *Journal of Geophysical Research-Solid Earth*, 108, B15. <https://doi.org/10.1029/2002JB002021>
- Salem, A. and Ravat, D. (2003) A combined analytic signal and Euler method (AN-EUL) for automatic interpretation of magnetic data. *Geophysics*, 68, 1952–1961.
- Schneider, W.A. (1978) Integral formulation for migration in 2 and 3 dimensions. *Geophysics*, 43, 49–76.
- Silva Dias, F.J.S., Barbosa, V.C.F. and Silva, J.B.C. (2011) Adaptive learning 3D gravity inversion for salt-body imaging. *Geophysics*, 76, 149–157.
- Smith, R.S. and Salem, A. (2005) Imaging depth, structure, and susceptibility from magnetic data: the advanced source-parameter imaging method. *Geophysics*, 70, L31–L38.
- Stadtler, C., Fichler, C., Hokstad, K., Myrlund, E.A., Wienecke, S. and Fotland, B. (2014) Improved salt imaging in a basin context by high resolution potential field data: Nordkapp Basin, Barents Sea. *Geophysical Prospecting*, 62, 615–630.
- Stavrev, P. (2006) Inversion of elongated magnetic anomalies using magnitude transforms. *Geophysical Prospecting*, 54, 153–166.
- Stavrev, P.Y. (1997) Euler deconvolution using differential similarity transformations of gravity or magnetic anomalies. *Geophysical Prospecting*, 45, 207–246.
- Thompson, D.T. (1982) Eulph - a new technique for making computer-assisted depth estimates from magnetic data. *Geophysics*, 47, 31–37.
- Ueda, T. and Zhdanov, M.S. (2008) Fast numerical methods for marine controlled-source electromagnetic (EM) survey data based on multigrid quasi-linear approximation and iterative EM migration. *Exploration Geophysics*, 39, 60–67.
- Wan, L. and Zhdanov, M.S. (2008) Focusing inversion of marine full-tensor gradiometry data in offshore geophysical exploration. In: *SEG Technical Program Expanded Abstracts 2008*, pp. 751–755. Society of Exploration Geophysicists, ISBN 1052–3812.
- Wan, L. and Zhdanov, M.S. (2013) Iterative migration of gravity and gravity gradiometry data. In: *SEG Technical Program Expanded Abstracts 2013*, pp. 1211–1215. Society of Exploration Geophysicists, ISBN 1052–3812.
- Yang, G.Y., Wang, J.H. and Yan, H.Z. (2019) Application of modeling inversion of Bouguer gravity anomalies to oil and gas exploration in the Erlan Basin. *Chinese Journal of Geophysics-Chinese Edition*, 62, 316–330.
- Yegorova, T.P., Stephenson, R.A., Kozlenko, V.G., Starostenko, V.I. and Legostaeva, O.V. (1999) 3-D gravity analysis of the Dniepr–Donets basin and Donbas Foldbelt, Ukraine. *Tectonophysics*, 313, 41–58.
- Zhdanov, M.S. (2002) *Geophysical Inverse Theory and Regularization Problems*. Elsevier, ISBN 0080532500.
- Zhdanov, M.S. (2009) *Geophysical Electromagnetic Theory and Methods*. Elsevier, ISBN 0080931766.
- Zhdanov, M.S. (2012) *Integral Transforms in Geophysics*. Springer Science & Business Media, ISBN 3642726283.
- Zhdanov, M.S. (2015) *Inverse Theory and Applications in Geophysics*. Elsevier, ISBN 044462712X.



- Zhdanov, M.S., Ellis, R. and Mukherjee, S. (2004) Three-dimensional regularized focusing inversion of gravity gradient tensor component data. *Geophysics*, 69, 925–937.
- Zhdanov, M.S., Liu, X. and Wilson, G. (2010) Potential field migration for rapid 3D imaging of entire gravity gradiometry surveys. *First Break*, 28, 47–51.
- Zhdanov, M.S., Han, M. and Wan, L. (2020) Joint iterative migration of surface and borehole gravity gradiometry data. *Active Geophysical Monitoring*, pp. 97–121. Elsevier.
- Zhdanov, M.S., Liu, X.J., Wilson, G.A. and Wan, L. (2011) Potential field migration for rapid imaging of gravity gradiometry data. *Geophysical Prospecting*, 59, 1052–1071.